

Adversarial Hospital-Invariant Feature Learning for WSI Patch Classification

Mengliang Zhang

Department of Computer Science and Engineering
The University of Texas at Arlington
Arlington, TX, U.S.A.
mxz3935@mavs.uta.edu

Jacob M. Luber

Department of Computer Science and Engineering
The University of Texas at Arlington
Arlington, TX, U.S.A.
jacob.luber@uta.edu

Abstract—Pathology foundation models (PFMs) have demonstrated remarkable potential in whole-slide image (WSI) diagnosis. However, pathology images from different hospitals often vary due to differences in scanning hardware and preprocessing styles, which may lead PFMs to inadvertently learn hospital-specific features, posing risks for clinical deployment. In this work, we present the first systematic study of domain bias in PFMs arising from hospital source characteristics. Specifically, we (1) construct a pipeline for quantifying domain bias in PFMs, (2) evaluate and compare the performance of multiple models, and (3) propose a lightweight adversarial framework that removes latent hospital-specific features from frozen representations without modifying the encoder itself. By introducing a trainable adapter and a domain classifier connected through a gradient reversal layer (GRL), our method learns task-discriminative yet domain-invariant representations. Experiments on multi-center histopathology datasets demonstrate that our approach substantially reduces domain predictability while maintaining or even improving disease classification performance, particularly in out-of-domain (unseen hospital) scenarios. Further analyses, including hospital detection and feature space visualization, confirm the effectiveness of our method in mitigating hospital bias. We will provide our code based on acceptance.

Index Terms—Pathology Image, Domain Bias, Foundation model.

I. INTRODUCTION

Whole-slide imaging (WSI) has become a key tool in digital pathology, enabling scalable analysis of gigapixel histopathology slides. In most downstream applications, WSIs are partitioned into small patches, and deep models—such as ResNet [3], Vision Transformer (ViT) [16], or foundation encoders like UNI [5] PLIP [13]—are employed to extract visual features for tasks including disease classification, tumor grading, and subtype analysis. These patch-level features form the backbone of many computational pathology pipelines.

However, a critical yet often underexplored challenge in this setting is the presence of domain-specific bias in the data. Patches collected from different hospitals or scanners frequently differ in staining protocols, image resolution, scanner artifacts, and tissue preparation. Such variations introduce spurious correlations into the learned representations, causing models to inadvertently rely on hospital-specific cues rather than true disease-related signals.

Even state-of-the-art pathology foundation models (PFMs), trained with self-supervised learning on large-scale datasets,

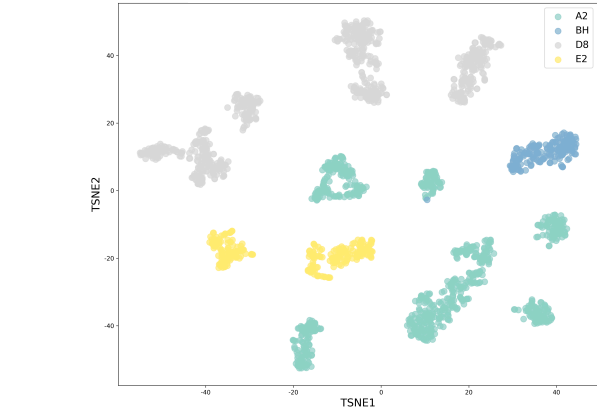


Fig. 1. t-SNE visualization of patch images from the TCGA-BRCA dataset using the Phikon [9] model, illustrating samples of the same disease collected from different hospitals. Colors indicate different hospital sources.

such as Phikon [9] and UNI [5] — exhibit a degree of domain bias. As illustrated in Figure 1, we perform t-SNE [14] clustering of patch embeddings from the TCGA-BRCA dataset using the Phikon [9] model, focusing on patches of the same disease but originating from different hospitals. Patches from the same source cluster closely together, indicating that the learned features retain hospital-specific information. This phenomenon poses risks for clinical deployment: the model may rely on latent hospital cues for diagnosis and could potentially leak hospital-source information from patch embeddings.

Several prior studies have explored domain bias in pathology foundation models (PFMs). Vaidya et al. [17] examined performance disparities of PFMs across different patient populations, while Lin et al. investigated inter-hospital variations and analyzed the limitations of DINO [20]-based feature learning. Edwin et al. [15] proposed a robustness metric for PFMs on patches from different hospital sources, using a KNN-based approach to measure the number of neighboring patches with the same hospital origin and disease label, thereby computing a robustness index. Other studies attempted to mitigate domain shifts through stain normalization techniques, such as Macenko [19] normalization, which standardizes patch color distributions across hospitals before feature extraction. How-

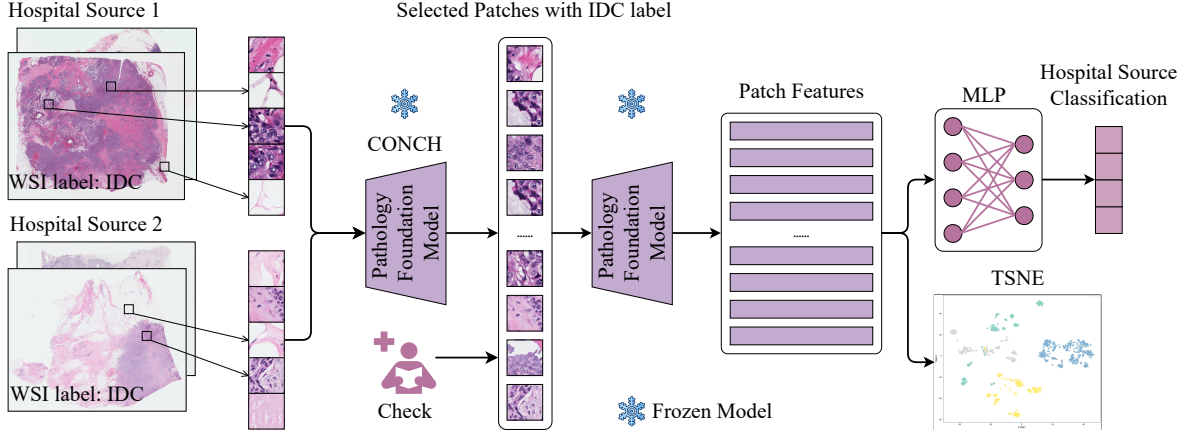


Fig. 2. Pipeline for evaluating hospital-domain bias in pathology foundation models. Only patches consistent with their WSI labels are used. A simple multi-layer perceptron (MLP) is trained to classify hospital sources, where higher accuracy indicates stronger domain bias.

ever, these methods are non-learnable, sensitive to parameter tuning, and only address low-level color differences, leaving other sources of domain variability—such as scanner artifacts or labeling inconsistencies—unresolved.

Another line of work leverages Canonical Correlation Analysis (CCA) to map patches from different hospitals into a shared feature space. Yet, these approaches have notable limitations. Edwin’s [15] metric cannot provide a dataset-level assessment of domain bias. CCA-based methods focus on feature alignment but overlook whether the aligned representations retain disease-discriminative power. Vaidya’s [17] approach requires additional LoRA [21] fine-tuning of PFMs and does not explicitly ensure the reduction of domain bias while preserving diagnostic performance.

In this work, we first establish a pipeline to evaluate the domain bias of pathology foundation models. We extract patches from the TCGA dataset and train two separate multi-layer perceptron (MLP) for disease classification and hospital-source classification. By measuring the hospital classification accuracy and AUC on the extracted patch features, we quantify the severity of domain bias in the model.

We then propose a lightweight adversarial framework to mitigate hospital-specific information in the extracted features. Our method introduces a trainable projection head, a domain classifier, and a disease classifier, where the domain classifier is connected to the projection head via a Gradient Reversal Layer (GRL). During backpropagation, the GRL reverses the gradient from the domain classifier, serving as adversarial feedback to suppress hospital-related cues while preserving disease-discriminative information throughout training. We validate our approach on multiple histopathology datasets. Experimental results demonstrate that the proposed adversarial training framework effectively suppresses hospital-specific signals and alleviates domain bias, while maintaining or even enhancing disease classification performance.

Our main contributions are as follows:

- 1) We establish a pipeline to identify and quantify domain

bias in features extracted by pathology foundation models with respect to hospital sources.

- 2) We propose a lightweight adversarial training framework that incorporates a Gradient Reversal Layer (GRL) to suppress hospital-related discriminative cues in image features without modifying the encoder.
- 3) Experiments on the TCGA dataset demonstrate that our method significantly suppresses latent hospital information in the extracted features while preserving disease classification performance.

II. RELATED WORKS

Recent advances in visual foundation models have had a significant impact on computational pathology, particularly in the design of patch-level feature extractors for whole-slide images (WSIs). Models such as CLIP [1] and DINO [20] have been widely adopted to extract transferable high-dimensional features from image patches. More recently, UNI [5] and CONCH [2] have achieved impressive results in various pathology tasks—including tumor classification, subtyping, and grading—under zero-shot and few-shot learning settings. These models are typically pretrained on large-scale natural image corpora or multimodal datasets and then used as frozen encoders. Despite their strong semantic capabilities, studies have observed that their features still encode dataset- or site-specific biases, including scanner artifacts and staining variations.

Several studies have explored hospital-domain bias in this context. Edwin et al. proposed a KNN-based robustness metric, which measures the number of neighboring patches sharing both the same hospital source and disease label to compute a robustness index. Vaidya et al. further introduced LoRA-based fine-tuning to adapt pathology foundation models to out-of-distribution (OOD) data. However, these approaches lack a systematic quantification-and-mitigation framework, leaving room for further optimization.

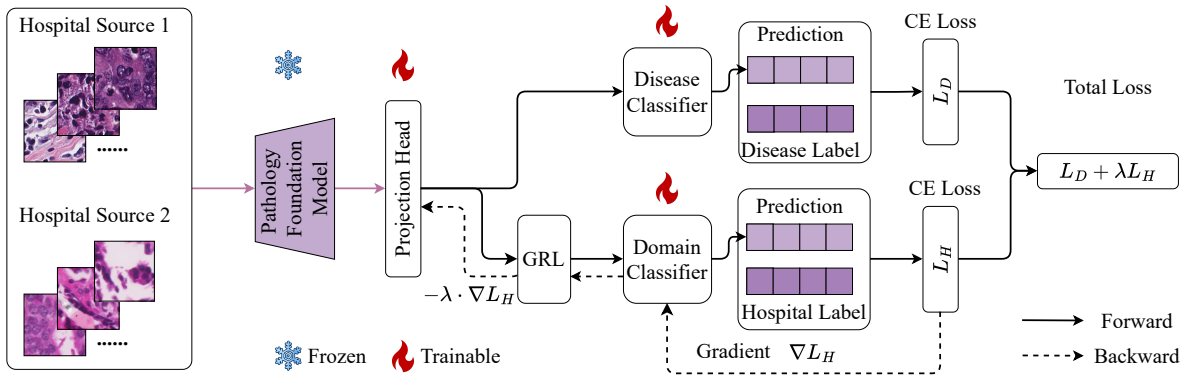


Fig. 3. Adversarial training framework.

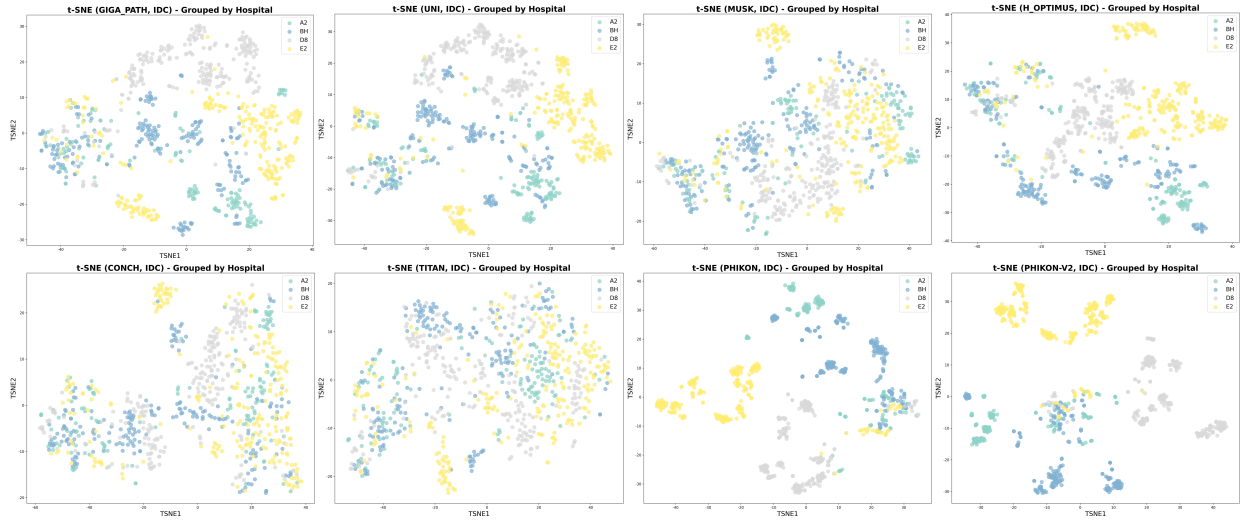


Fig. 4. t-SNE visualizations of patch features from different models for IDC in the TCGA-BRCA dataset.

III. METHODOLOGY

A. Patch Selection

For a given WSI collection, we first construct a cohort by filtering WSIs using available demographic information (e.g., sex and age) to select cases with comparable clinical conditions. This step helps reduce the potential confounding effects of demographic factors on WSI disease features. For each hospital and each disease category, we select a specified number of WSIs, striving to maintain balanced sample sizes across hospitals and disease classes.

For each WSI, we follow the tissue segmentation strategy from CLAM [12], applying Otsu thresholding to automatically distinguish tissue regions from background. This step generates a tissue mask used for subsequent patch extraction. Within the identified tissue regions, we extract fixed-size patches using a sliding window with a predefined grid pattern. Each extracted patch undergoes quality control, including checks for tissue coverage and minimum effective area, ensuring that the patches retain sufficient diagnostic value.

Next, we leverage the CONCH [2] model to further refine the patch set by ensuring consistency between patch-level and WSI-level labels, as shown in Figure 2. This choice is motivated by our preliminary observations that CONCH embeddings produce t-SNE distributions with less pronounced hospital clustering for patches of the same disease across different sites. We perform zero-shot patch classification using CONCH, obtain the top-1 predicted label and its probability, and select only those patches where (1) the predicted label probability exceeds a predefined threshold and (2) the label matches the WSI-level ground truth. Manual inspection of sampled patches is additionally performed to ensure label accuracy and consistency.

In Figure 2, for the extracted patches, we train a simple multi-layer perceptron (MLP) to perform classification based on both hospital source and disease label. Classification performance is evaluated using accuracy, AUC, and F1 score.

For the hospital-source classification task, higher accuracy indicates that hospital origin can be easily inferred from the extracted features, reflecting stronger domain bias in the corresponding pathology foundation model. In contrast, for

the disease classification task, higher accuracy suggests that the foundation model achieves better disease-discriminative performance.

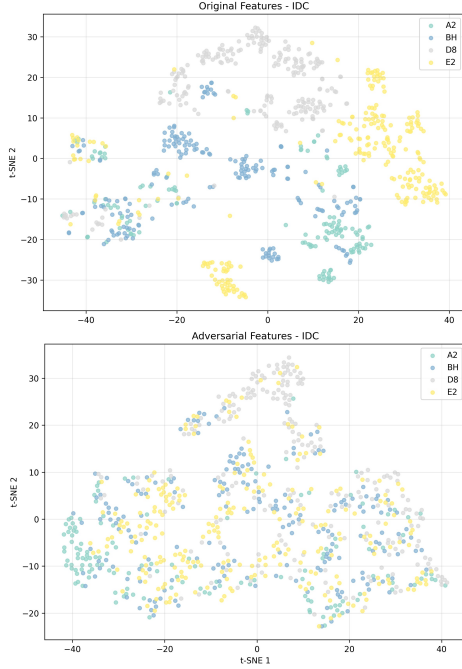


Fig. 5. t-SNE clustering results of the original patch features using the UNI model (top) and the t-SNE clustering results of the features after adversarial training (bottom). All patches share the same label, while points in different colors correspond to different hospitals.

B. Adversarial Method

We propose a lightweight adversarial training framework to suppress latent hospital-specific information in the features extracted by pathology foundation models, while preserving disease-discriminative signals. The framework incorporates a trainable projection head, a domain classifier, and a disease classifier, where the domain classifier is connected to the projection head via a Gradient Reversal Layer (GRL). During backpropagation, the GRL reverses the gradients from the domain classifier, providing adversarial feedback that discourages hospital-specific cues in the learned representation.

a) Problem Setup.: Let $\mathcal{D} = \{(x_i, y_i, d_i)\}_{i=1}^N$ denote a dataset of WSI patches, where $x_i \in \mathbb{R}^{H \times W \times 3}$ is an image patch, y_i is the disease label, and d_i is the domain label indicating the source hospital. We assume access to a frozen encoder $E(\cdot)$ (e.g., UNI or CONCH), which maps x_i to a feature vector

$$\mathbf{f}_i = E(x_i) \in \mathbb{R}^D. \quad (1)$$

Our objective is to learn a transformed representation $\mathbf{z}_i = A(\mathbf{f}_i)$ such that:

- \mathbf{z}_i retains disease-discriminative information for predicting y_i ;
- \mathbf{z}_i suppresses hospital-specific information, preventing reliable prediction of d_i .

C. Model Architecture

The model comprises four components:

a) Frozen Encoder $E(x)$: A pretrained visual encoder that extracts patch-level features. Its parameters remain frozen during training.

b) Projection Head $A(\mathbf{f})$: A lightweight MLP that projects the encoder feature \mathbf{f}_i into a lower-dimensional representation \mathbf{z}_i :

$$\mathbf{z}_i = A(E(x_i)) \in \mathbb{R}^{D'}. \quad (2)$$

c) Disease Classifier $C_y(\mathbf{z})$: Predicts the disease label from the projected feature:

$$\hat{y}_i = C_y(\mathbf{z}_i). \quad (3)$$

d) Domain Classifier $C_d(\cdot)$ with GRL: Predicts the hospital source from \mathbf{z}_i after passing through a GRL:

$$\hat{d}_i = C_d(\text{GRL}(\mathbf{z}_i)). \quad (4)$$

D. Gradient Reversal Layer (GRL)

In Figure 3, the GRL acts as the identity function in the forward pass, $\text{GRL}(\mathbf{z}_i) = \mathbf{z}_i$, but reverses and scales the gradients in the backward pass:

$$\frac{\partial \mathcal{L}}{\partial \mathbf{z}_i} \leftarrow -\lambda \cdot \frac{\partial \mathcal{L}}{\partial \mathbf{z}_i}, \quad (5)$$

where $\lambda \geq 0$ controls the adversarial strength. This forces the projection head to produce features that remain informative for disease prediction while becoming uninformative for hospital-source classification.

E. Loss Function

The total loss is a weighted sum of disease and domain losses:

$$\mathcal{L}_{\text{total}} = \mathcal{L}_D + \lambda \cdot \mathcal{L}_H, \quad (6)$$

where λ aligns with the GRL scaling factor.

a) Disease Loss.: We employ standard cross-entropy (CE) loss for disease prediction:

$$\mathcal{L}_D = \frac{1}{N} \sum_{i=1}^N \text{CE}(C_y(\mathbf{z}_i), y_i). \quad (7)$$

b) Domain Loss.: The domain classifier is trained to predict the hospital source using CE loss:

$$\mathcal{L}_H = \frac{1}{N} \sum_{i=1}^N \text{CE}(C_d(\text{GRL}(\mathbf{z}_i)), d_i). \quad (8)$$

During training, only the projection head and the two classifiers are updated, while the encoder remains frozen. At inference time, the GRL and domain classifier are discarded, and the final prediction is obtained as:

$$\hat{y}_i = C_y(A(E(x_i))) = C_y(\mathbf{z}_i). \quad (9)$$

TABLE I
PERFORMANCE OF DIFFERENT MODELS ON HOSPITAL-SOURCE CLASSIFICATION BEFORE AND AFTER ADVERSARIAL TRAINING. WE REPORT MEAN \pm STANDARD DEVIATION FOR ACCURACY, AUC, AND F1.

Model	Method	Accuracy(\pm std)	AUC(\pm std)	F1(\pm std)
CONCH	MLP	0.6049 \pm 0.0573	0.8442 \pm 0.0299	0.5459 \pm 0.0787
	Adversarial	0.2250 \pm 0.1675	0.5900 \pm 0.1309	0.1678 \pm 0.1175
GIGA_PATH	MLP	0.6843 \pm 0.1178	0.9104 \pm 0.0388	0.6440 \pm 0.1217
	Adversarial	0.2427 \pm 0.1888	0.5719 \pm 0.1104	0.1411 \pm 0.1276
H_OPTIMUS	MLP	0.8064 \pm 0.0875	0.9652 \pm 0.0167	0.7753 \pm 0.1214
	Adversarial	0.3384 \pm 0.1570	0.6736 \pm 0.1333	0.2288 \pm 0.1040
MUSK	MLP	0.6886 \pm 0.0943	0.8980 \pm 0.0448	0.6283 \pm 0.1002
	Adversarial	0.2883 \pm 0.1620	0.5000 \pm 0.0000	0.1051 \pm 0.0545
PHIKON	MLP	0.8463 \pm 0.0735	0.9805 \pm 0.0105	0.8105 \pm 0.0969
	Adversarial	0.4533 \pm 0.1168	0.7349 \pm 0.1062	0.3590 \pm 0.1449
PHIKON-V2	MLP	0.9161 \pm 0.0282	0.9918 \pm 0.0036	0.8874 \pm 0.0684
	Adversarial	0.4760 \pm 0.1861	0.7629 \pm 0.1707	0.4372 \pm 0.2146
RESNET50	MLP	0.6019 \pm 0.0848	0.8305 \pm 0.0537	0.5460 \pm 0.0898
	Adversarial	0.2544 \pm 0.1611	0.5124 \pm 0.0248	0.0947 \pm 0.0531
TITAN	MLP	0.5667 \pm 0.0699	0.8226 \pm 0.0395	0.5134 \pm 0.0669
	Adversarial	0.2289 \pm 0.1124	0.5446 \pm 0.0891	0.0924 \pm 0.0450
UNI	MLP	0.7836 \pm 0.0730	0.9483 \pm 0.0317	0.7416 \pm 0.0954
	Adversarial	0.2166 \pm 0.1130	0.5788 \pm 0.0630	0.0875 \pm 0.0377
UNI2-H	MLP	0.7860 \pm 0.0951	0.9571 \pm 0.0199	0.7569 \pm 0.1072
	Adversarial	0.1928 \pm 0.1079	0.5142 \pm 0.0497	0.1045 \pm 0.0681
VIRCHOW	MLP	0.7133 \pm 0.1507	0.9095 \pm 0.0675	0.6794 \pm 0.1574
	Adversarial	0.1335 \pm 0.1062	0.4938 \pm 0.0311	0.0558 \pm 0.0405

TABLE II
STATISTICS OF FILTERED PATCHES BY DISEASE TYPE AND HOSPITAL SOURCE IN TCGA-BRCA.

Category	Name	Filtered Count
Disease	IDC	2,146
Disease	ILC	1,883
Hospital	E2	911
Hospital	A2	1,221
Hospital	D8	1,220
Hospital	BH	677
Total	All	4,029

IV. EXPERIMENT

A. Setup

As an illustrative example, we focus on whole-slide image (WSI) samples from the TCGA-BRCA dataset [22]. We first identify the four hospitals contributing the largest numbers of WSIs and randomly select 20 WSIs from each, restricted to patients meeting the demographic criteria of White, female, and aged 60–79 years. From each selected WSI, we uniformly sample 500 image patches of size 256×256 at a $40\times$ magnification. These initial patches are subsequently filtered using the CONCH foundation model: only patches whose zero-shot predicted label matches the WSI-level ground truth with a

confidence score of at least 0.8 are retained. After filtering, a total of 4,029 high-confidence patches remain, corresponding to two disease categories: Invasive Ductal Carcinoma (IDC) and Invasive Lobular Carcinoma (ILC).

Since randomly sampled patches may not always reflect the WSI-level diagnosis (e.g., a WSI labeled IDC may contain normal tissue), we adopt the CONCH foundation model [2], which provides strong zero-shot disease classification, to filter the patches. We retain only those patches whose predicted patch-level label matches the WSI label and whose prediction confidence exceeds 0.8.

The filtered patches are then used to extract features from a set of representative pathology foundation models, including ResNet-50 [3], Giga-Path [4], UNI [5], UNI2-H [5], CONCH [2], TITAN [6], MUSK [7], H-Optimus-0 [8], Phikon [9], Phikon-v2 [10], and Virchow [11]. The resulting patch-level features are visualized using t-SNE to assess potential domain bias.

For model training, we use 30 epochs with a batch size of 64, set the adversarial strength λ to 0.5, and use a projection head with a hidden dimension of 512. Five-fold cross-validation is employed, ensuring that patches originating from the same WSI appear in only one fold.

For the TCGA-LUAD [23] and TCGA-LUSC [24] datasets, we apply the same demographic criteria and patch extraction strategy. The disease labels are Lung Adenocarcinoma

TABLE III
PERFORMANCE COMPARISON OF DIFFERENT MODELS WITH MLP AND ADVERSARIAL METHODS. WE REPORT MEAN \pm STANDARD DEVIATION FOR ACCURACY, AUC, AND F1. THE DISEASE CLASSIFICATION RESULTS OF THE CONCH MODEL ARE PROVIDED FOR REFERENCE ONLY, AS CONCH WAS USED FOR PATCH PRE-FILTERING.

Model	Method	Accuracy(\pm std)	AUC(\pm std)	F1(\pm std)
CONCH	MLP	1.0000 \pm 0.0000	1.0000 \pm 0.0000	1.0000 \pm 0.0000
	Adversarial	1.0000 \pm 0.0000	1.0000 \pm 0.0000	1.0000 \pm 0.0000
GIGA_PATH	MLP	0.9148 \pm 0.0307	0.9746 \pm 0.0063	0.9091 \pm 0.0336
	Adversarial	0.9227 \pm 0.0220	0.9611 \pm 0.0120	0.9169 \pm 0.0271
H_OPTIMUS	MLP	0.9062 \pm 0.0536	0.9731 \pm 0.0229	0.9020 \pm 0.0542
	Adversarial	0.9173 \pm 0.0418	0.9546 \pm 0.0255	0.9136 \pm 0.0428
MUSK	MLP	0.9391 \pm 0.0121	0.9877 \pm 0.0029	0.9359 \pm 0.0128
	Adversarial	0.9398 \pm 0.0127	0.9748 \pm 0.0073	0.9366 \pm 0.0127
PHIKON	MLP	0.8536 \pm 0.0915	0.9412 \pm 0.0440	0.8403 \pm 0.0955
	Adversarial	0.8763 \pm 0.0921	0.9259 \pm 0.0579	0.8695 \pm 0.0919
PHIKON-V2	MLP	0.8701 \pm 0.0755	0.9470 \pm 0.0433	0.8561 \pm 0.0847
	Adversarial	0.8596 \pm 0.0856	0.9365 \pm 0.0414	0.8459 \pm 0.0908
RESNET50	MLP	0.8512 \pm 0.0282	0.9307 \pm 0.0202	0.8420 \pm 0.0331
	Adversarial	0.8580 \pm 0.0472	0.9312 \pm 0.0327	0.8499 \pm 0.0501
TITAN	MLP	0.9389 \pm 0.0108	0.9831 \pm 0.0067	0.9349 \pm 0.0136
	Adversarial	0.9294 \pm 0.0155	0.9817 \pm 0.0079	0.9249 \pm 0.0180
UNI	MLP	0.9337 \pm 0.0338	0.9822 \pm 0.0138	0.9291 \pm 0.0369
	Adversarial	0.9278 \pm 0.0368	0.9613 \pm 0.0363	0.9230 \pm 0.0400
UNI2-H	MLP	0.9219 \pm 0.0360	0.9823 \pm 0.0083	0.9182 \pm 0.0369
	Adversarial	0.9187 \pm 0.0432	0.9700 \pm 0.0199	0.9151 \pm 0.0438
VIRCHOW	MLP	0.9100 \pm 0.0505	0.9829 \pm 0.0076	0.9054 \pm 0.0518
	Adversarial	0.9049 \pm 0.0487	0.9733 \pm 0.0134	0.8993 \pm 0.0500

(LUAD) and Lung Squamous Cell Carcinoma (LUSC), respectively.

B. Results

We conducted experiments on the TCGA-BRCA, TCGA-LUAD, and TCGA-LUSC datasets to comprehensively evaluate pathology foundation models from multiple perspectives, including t-SNE feature visualization, disease classification performance, and hospital-source classification performance.

Figure 4 shows a t-SNE visualization of patch features labeled as IDC in the TCGA-BRCA dataset, where points of different colors correspond to different hospital sources. Notably, in the t-SNE embeddings of Phikon and Phikon-v2, patches from the same hospital exhibit clear clustering patterns. This observation indicates that the features extracted by these models retain substantial hospital-specific information, reflecting the presence of domain bias in their representations.

Table I further summarizes the hospital-source classification performance of various models. In the *Method* column, “MLP” denotes the classification performance obtained by training an MLP on the original patch features prior to adversarial training, while “Adversarial” represents the performance after applying our adversarial training framework. For reference, we also include ResNet-50 as a baseline model that has not been pretrained on pathology images. Interestingly, Phikon and

Phikon-v2 achieve the highest accuracy and AUC in hospital-source classification, which is consistent with the strong clustering of hospital-specific features observed in the t-SNE plots. Even the ResNet-50 baseline demonstrates a non-trivial ability to distinguish hospital sources, suggesting that latent hospital-specific cues are embedded in the patch features and can be exploited even without pathology-specific pretraining. In contrast, the CONCH model—used in our pipeline for patch filtering—exhibits comparatively lower hospital-source classification accuracy, implying that it is more robust to hospital-related domain bias. Following adversarial training, all models exhibit a marked reduction in their hospital-source classification capability, with the AUC approaching 0.5, which corresponds to random guessing. This result confirms that our adversarial framework effectively suppresses latent hospital-specific cues in the learned representations.

Table III presents the disease classification performance of the evaluated models. In the *Method* column, “MLP” denotes the classification performance obtained by training an MLP on the original patch features prior to adversarial training, while “Adversarial” represents the performance after applying our adversarial training framework. Since patch selection was performed using the CONCH model, its reported performance reaches 1.0, this does not imply that CONCH achieves perfect disease classification in general.

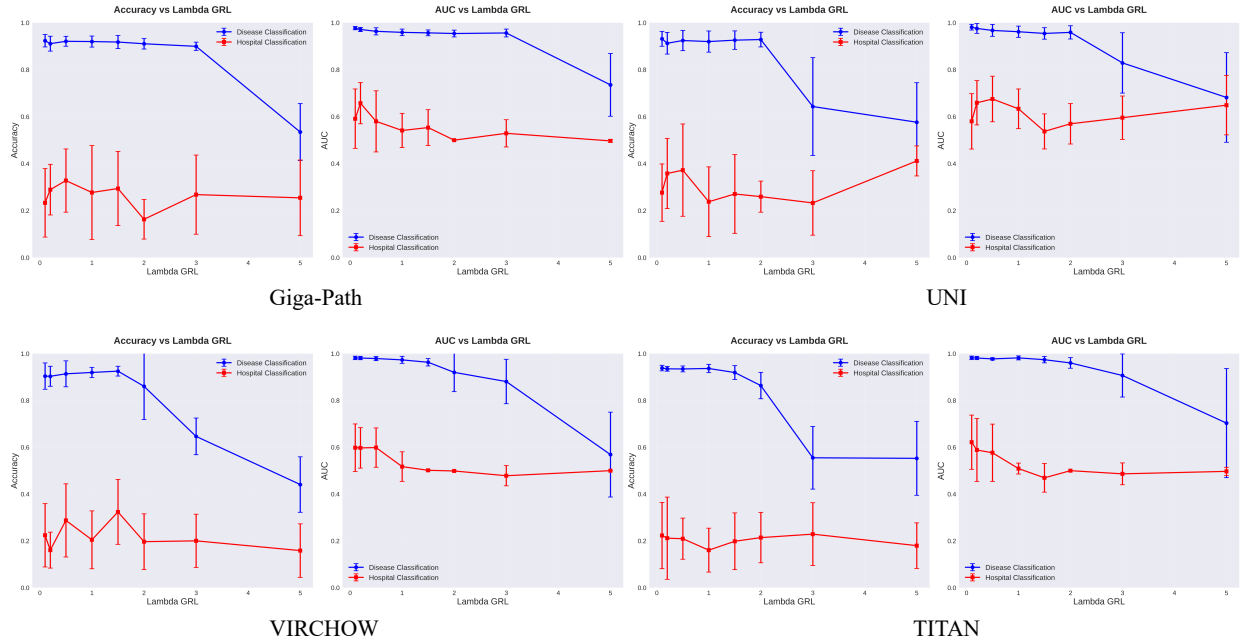


Fig. 6. Changes in accuracy and AUC for disease classification and hospital-source classification under different values of λ . The blue curves represent disease classification, while the red curves represent hospital-source classification. The vertical lines indicate standard deviation error bars.

Other models also demonstrate strong disease classification performance. For example, ResNet-50 achieves an AUC of approximately 0.9, which can be partially attributed to the fact that the selected patches contain highly distinguishable pathological features. Moreover, across all models, the disease classification performance after adversarial training remains comparable to that of the pre-training MLPs, indicating that our adversarial framework effectively suppresses hospital-specific information without degrading disease-discriminative capability.

We compared color distortion and a CCA-based method using the UNI model. As shown in Table IV, color distortion only slightly reduces domain bias. Although CCA effectively removes hospital-specific features by aligning feature spaces, it substantially harms disease classification performance, making it unsuitable for this task.

We also evaluated the UNI model on TCGA-LUAD and TCGA-LUSC datasets before and after adversarial training (Table V). Post-training, hospital-source classification metrics drop significantly, while disease classification remains stable, demonstrating the robustness and generalizability of our adversarial framework.

C. Parameter Study

In adversarial training, the parameter λ controls the trade-off between suppressing hospital-specific features and preserving disease-discriminative information. In Figure 6, a small λ (e.g., 0.1) only weakly suppresses domain cues, while a moderate value (e.g., 1.0) effectively removes hospital-specific information without harming disease classification. Excessively large λ (e.g., 5.0) degrades disease performance, indicating

suppression of useful features. Based on the result, we choose a moderate $\lambda = 1.0$ achieves the balance.

V. CONCLUSION

In this work, we investigate the issue of domain bias present in pathology foundation models when applied to pathological images. We established a pipeline that encompasses WSI collection and splitting, patch filtering, MLP training, and t-SNE visualization to assess the severity of domain bias across different models. Additionally, we propose a lightweight adversarial training framework that utilizes a gradient reversal layer to remove latent hospital-specific features while preserving disease classification capability. Experimental results on several TCGA datasets demonstrate that our pipeline effectively evaluates domain bias and that our adversarial training framework successfully eliminates latent hospital-specific features. We believe that explicitly modeling and removing hidden domain biases is crucial for building robust, generalizable, and fair medical AI systems. Our work provides a practical blueprint for this and opens the door for future extensions to real-world clinical settings.

ACKNOWLEDGMENT

We gratefully acknowledge TCGA for providing publicly available datasets and the developers of various pathology foundation models for releasing their pretrained weights. Their contributions to data and model sharing were instrumental in enabling this research. All patient data were obtained from the publicly available Cancer Genome Atlas (TCGA) program under dbGaP Data Use Certification. The datasets are fully de-identified, and no additional institutional review board (IRB) approval was required.

TABLE IV

PERFORMANCE OF DIFFERENT METHODS ON HOSPITAL-SOURCE AND DISEASE CLASSIFICATION TASKS USING UNI MODEL. WE REPORT MEAN \pm STANDARD DEVIATION FOR ACCURACY, AUC, AND F1.

Task	Method	Accuracy(\pm std)	AUC(\pm std)	F1(\pm std)
Hospital	MLP	0.7836 \pm 0.0730	0.9483 \pm 0.0317	0.7416 \pm 0.0954
	Color Distortion	0.7561 \pm 0.0875	0.9142 \pm 0.0309	0.7229 \pm 0.0875
	CCA	0.2289 \pm 0.0419	0.4504 \pm 0.0388	0.1440 \pm 0.0217
	Adversarial	0.2166 \pm 0.1130	0.5788 \pm 0.0630	0.0875 \pm 0.0377
Disease	MLP	0.9337 \pm 0.0338	0.9822 \pm 0.0138	0.9291 \pm 0.0369
	Color Distortion	0.9120 \pm 0.0359	0.9200 \pm 0.0309	0.8978 \pm 0.0375
	CCA	0.4694 \pm 0.0218	0.4704 \pm 0.0188	0.4840 \pm 0.0197
	Adversarial	0.9278 \pm 0.0368	0.9613 \pm 0.0363	0.9230 \pm 0.0400

TABLE V

EVALUATION OF DIFFERENT METHODS FOR HOSPITAL-SOURCE AND DISEASE CLASSIFICATION TASKS USING THE UNI MODEL ON THE TCGA-LUAD AND TCGA-LUSC DATASETS. REPORTED METRICS INCLUDE MEAN \pm STANDARD DEVIATION FOR ACCURACY, AUC, AND F1 SCORE.

Task	Method	Accuracy(\pm std)	AUC(\pm std)	F1(\pm std)
Hosp	MLP	0.7855 \pm 0.0438	0.8883 \pm 0.0212	0.7845 \pm 0.0247
	Adversarial	0.2246 \pm 0.1332	0.5568 \pm 0.0450	0.1875 \pm 0.0377
Disease	MLP	0.9353 \pm 0.0192	0.9748 \pm 0.0132	0.9288 \pm 0.0369
	Adversarial	0.9324 \pm 0.0183	0.9646 \pm 0.0114	0.9280 \pm 0.0208

REFERENCES

- [1] A. Radford et al., "Learning Transferable Visual Models from Natural Language Supervision," in Proceedings of the 38th international conference on machine learning, M. Meila and T. Zhang, Eds., in Proceedings of machine learning research, vol. 139. PMLR, July 2021, pp. 8748–8763. [Online]. Available: <https://proceedings.mlr.press/v139/radford21a.html>
- [2] M. Y. Lu et al., "A Visual-Language Foundation Model for Computational Pathology," Nat Med, vol. 30, no. 3, pp. 863–874, Mar. 2024, doi: 10.1038/s41591-024-02856-4.
- [3] K. He, X. Zhang, S. Ren, and J. Sun, "Deep Residual Learning for Image Recognition," in 2016 IEEE Conference on Computer Vision and Pattern Recognition (CVPR), Las Vegas, NV, USA: IEEE, June 2016, pp. 770–778. doi: 10.1109/CVPR.2016.90.
- [4] H. Xu et al., "A Whole-Slide Foundation Model for Digital Pathology from Real-World Data," Nature, vol. 630, no. 8015, pp. 181–188, June 2024, doi: 10.1038/s41586-024-07441-w.
- [5] R. J. Chen et al., "Towards a General-Purpose Foundation Model for Computational Pathology," Nat Med, vol. 30, no. 3, pp. 850–862, Mar. 2024, doi: 10.1038/s41591-024-02857-3.
- [6] T. Ding et al., "Multimodal Whole Slide Foundation Model for Pathology," Nov. 29, 2024, arXiv: arXiv:2411.19666. doi: 10.48550/arXiv.2411.19666.
- [7] J. Xiang et al., "A Vision-Language Foundation Model for Precision Oncology," Nature, vol. 638, no. 8051, pp. 769–778, Feb. 2025, doi: 10.1038/s41586-024-08378-w.
- [8] C. Saillard et al., H-optimus-0. (2024). [Online]. Available: <https://github.com/bioptimus/releases/tree/main/models/h-optimus/v0>
- [9] A. Filiot et al., "Scaling Self-Supervised Learning for Histopathology with Masked Image Modeling," Sept. 14, 2023, medRxiv. doi: 10.1101/2023.07.21.23292757.
- [10] A. Filiot, P. Jacob, A. M. Kain, and C. Saillard, "Phikon-v2, A large and public feature extractor for biomarker prediction," Sept. 13, 2024, arXiv: arXiv:2409.09173. doi: 10.48550/arXiv.2409.09173.
- [11] E. Vorontsov et al., "A Foundation Model for Clinical-Grade Computational Pathology and Rare Cancers Detection," Nat Med, vol. 30, no. 10, pp. 2924–2935, Oct. 2024, doi: 10.1038/s41591-024-03141-0.
- [12] M. Y. Lu, D. F. K. Williamson, T. Y. Chen, R. J. Chen, M. Barbieri, and F. Mahmood, "Data-Efficient and Weakly Supervised Computational Pathology on Whole-Slide Images," Nature Biomedical Engineering, vol. 5, no. 6, pp. 555–570, June 2021, doi: 10.1038/s41551-020-00682-w.
- [13] Z. Huang, F. Bianchi, M. Yuksekgonul, T. J. Montine, and J. Zou, "A Visual-Language Foundation Model for Pathology Image Analysis Using Medical Twitter," Nat Med, vol. 29, no. 9, pp. 2307–2316, Sept. 2023, doi: 10.1038/s41591-023-02504-3.
- [14] L. van der Maaten and G. Hinton, "Visualizing data using t-SNE," Journal of Machine Learning Research, vol. 9, no. 86, pp. 2579–2605, 2008.
- [15] E. D. de Jong, E. Marcus, and J. Teuwen, "Current Pathology Foundation Models Are Unrobust to Medical Center Differences," Feb. 01, 2025, arXiv: arXiv:2501.18055. doi: 10.48550/arXiv.2501.18055.
- [16] A. Dosovitskiy et al., "An Image is Worth 16x16 Words: Transformers for Image Recognition at Scale," in arXiv:2010.11929 [cs], ICLR, June 2021. Accessed: Mar. 14, 2022. [Online]. Available: <http://arxiv.org/abs/2010.11929>
- [17] A. Vaidya et al., "Demographic Bias in Misdiagnosis by Computational Pathology Models," Nature Medicine, vol. 30, no. 4, pp. 1174–1190, Apr. 2024, doi: 10.1038/s41591-024-02885-z.
- [18] W. Lin, S. Liu, R. Zhu, and L. Wang, "Unveiling Institution-Specific Bias in Pathology Foundation Models: Detriments, Causes, and Potential Solutions," Feb. 24, 2025, arXiv: arXiv:2502.16889. doi: 10.48550/arXiv.2502.16889.
- [19] M. Macenko et al., "A Method for Normalizing Histology Slides for Quantitative Analysis," in 2009 IEEE International Symposium on Biomedical Imaging: From Nano to Macro, July 2009, pp. 1107–1110. doi: 10.1109/ISBI.2009.5193250.
- [20] M. Caron et al., "Emerging Properties in Self-Supervised Vision Transformers," May 24, 2021, arXiv: arXiv:2104.14294. doi: 10.48550/arXiv.2104.14294.
- [21] E. J. Hu, Y. Shen, P. Wallis, Z. Allen-Zhu, Y. Li, S. Wang, L. Wang, and W. Chen, "LoRA: Low-rank adaptation of large language models," in *Proc. Int. Conf. Learning Representations (ICLR)*, 2022.
- [22] The Cancer Genome Atlas Breast Invasive Carcinoma Collection (TCGA-BRCA) (Version 3), The Cancer Imaging Archive, 2016. <https://doi.org/10.7937/K9/TCIA.2016.AB2NAZRP>
- [23] The Cancer Genome Atlas Lung Adenocarcinoma Collection (TCGA-LUAD), The Cancer Imaging Archive. <https://doi.org/10.7937/TCIA.2018.p3311qfd>
- [24] The Cancer Genome Atlas Lung Squamous Cell Carcinoma Collection (TCGA-LUSC), The Cancer Imaging Archive. <https://doi.org/10.7937/TCIA.2018.hp6yaq7i>